chemosensors

MDPI

Article

Optical Sensing of Molecular Oxygen (O_2) via Metal Oxide Photoluminescence: A Comparative Study of TiO_2, SnO_2 and ZnO

Ambra Fioravanti [1], Pietro Marani [1], Sara Morandi [2], Laura Giordano [3], Pasqualino Maddalena [4], Maria Cristina Carotta [1,*] and Stefano Lettieri [5,*]

1 Institute of Sciences and Technologies for Sustainable Energy and Mobility, National Research Council (STEMS-CNR), Via Canal Bianco 28, 44124 Ferrara, Italy; ambra.fioravanti@stems.cnr.it (A.F.); pietro.marani@stems.cnr.it (P.M.)
2 Department of Chemistry, University of Torino, Via P. Giuria 7, 10125 Turin, Italy; sara.morandi@unito.it
3 Institute of Marine Sciences, National Research Council (ISMAR-CNR), Calata Porta di Massa, 80133 Naples, Italy; laura.giordano@cnr.it
4 Department of Physics, Università degli Studi di Napoli "Federico II", Via Cupa Cintia 21, 80126 Naples, Italy; pasqualino.maddalena@unina.it
5 Institute for Applied Sciences and Intelligent Systems "E. Caianiello", National Research Council (ISASI-CNR), Via Cupa Cintia 21, 80126 Naples, Italy
* Correspondence: mc.carotta@imamoter.cnr.it (M.C.C.); stefano.lettieri@isasi.cnr.it (S.L.)

Abstract: A comparative study is presented on the photoluminescence (PL) response toward molecular oxygen (O_2) in tin dioxide (SnO_2), zinc oxide (ZnO) and titanium dioxide (TiO_2) nanoparticles. The findings show that both PL enhancement and PL quenching can be observed on different materials, arguably depending on the spatial localization of the defects responsible for the PL emission in each different oxide. No significant results are evidenced for SnO_2 nanoparticles. ZnO with red/orange emission shown an O_2-induced PL enhancement, suggesting that the radiative emission involves holes trapped in surface vacancy oxygen centers. While the ZnO results are scientifically interesting, its performances are inferior to the ones shown by TiO_2, which exhibits the most interesting response in terms of sensitivity and versatility of the response. In particular, O_2 concentrations in the range of few percent and in the range of a few tenths of a part per million are both detectable through the same mixed-phase TiO_2 sample, whose rutile phase gives a reversible and fast response to larger (0.4–2%) O_2 concentration while its anatase phase is usable for detection in the 25–75 ppm range. The data for rutile TiO_2 suggest that its surfaces host deeply trapped electrons at large densities, allowing good sensitivities and, more notably, a relatively unsaturated response at large concentrations. Future work is expected to improve the understanding and modeling of the photophysical framework that lies behind the observations.

Keywords: titanium dioxide; zinc oxide; tin dioxide; photoluminescence; optical sensors; oxygen sensors; rutile; anatase; crystal defects

Citation: Fioravanti, A.; Marani, P.; Morandi, S.; Giordano, L.; Maddalena, P.; Carotta, M.C.; Lettieri, S. Optical Sensing of Molecular Oxygen (O_2) via Metal Oxide Photoluminescence: A Comparative Study of TiO_2, SnO_2 and ZnO. *Chemosensors* **2021**, *9*, 163. https://doi.org/10.3390/chemosensors9070163

Academic Editor: José Manuel Costa Fernández

Received: 28 May 2021
Accepted: 24 June 2021
Published: 28 June 2021

1. Introduction

In this work, we investigate the interplay between molecular oxygen (O_2) adsorption and photoluminescence (PL) emission of selected metal oxide (MOX) nanoparticles, aiming to shed light on the potentialities vs. limitations in employing such materials as optical O_2 sensors and to discuss the photophysical framework that lies behind the observations.

It is well-known that many MOXs, including those considered in this work, are of great importance not only in the field of chemosensors but also for photocatalytic applications. This point is relevant in relation to the motivations of the present study, which can be summarized by two arguments. The first relates to the applicative interests in developing O_2 sensors, while the second underlines the scientific importance of elucidating the role of O_2 in heterogeneous photocatalysts.

Oxygen sensing can be implemented in terms of detection of O_2 in gas phase or of dissolved oxygen (DO) in water. Measurements of concentration for the latter are of great importance for monitoring the health of marine environments and of water pollution in general [1]. Furthermore, the control of DO content is a relevant issue in biology: to mention a few examples, hyperoxia has been related to formation of reactive oxygen species and subsequent cell death [2,3]. Additionally, hypoxia and re-oxygenation enhance the proliferation, invasiveness and metastatic potential of tumor cells [4,5].

While electrochemical cells (i.e., Clark electrodes) [6] have been used for several years for DO analyses, approaches and technologies relying on optical measurements are also largely used thanks to peculiar advantages such as the fact that they do not consume oxygen and can be relatively portable and easy to miniaturize [7–10]. The optical sensing of O_2 typically relies on the use of photoluminescent organo-metallic coordination complexes, whose intensity is dependent on the local O_2 concentration because of "static quenching" phenomena. As a result, the O_2 concentration is correlated to the PL intensity of the optical sensing material (or "oxygen indicator") by the Stern–Volmer quenching relation:

$$I_0/I = 1 + k_{SV}[O_2] \quad (1)$$

where I_0 and I are the luminescence intensity in absence and presence of oxygen (or, more generally, in presence of the quencher), $[O_2]$ is the oxygen concentration and k_{SV} is the Stern–Volmer constant related to the luminescence lifetime and the probability of quenching interaction [11].

Metal–ligand coordination complexes are widely used for this purpose. However, it is important to highlight that inorganic semiconductors can also exhibit oxygen-dependent (and—more generally—gas-dependent properties) that can often be exploited in either optical and/or electrical responses [12–20]. Among inorganic semiconductors exploitable for chemical sensing there are of course several MOXs which are not only the primary materials of choice for realization of chemoresistive sensors but are also suitable for optical sensing. Optochemical sensing by MOXs includes PL-based detection [21–25] but also other techniques: for example, MOXs can be used to prepare photonic crystals or metasurfaces [26–29] finding applications in chemical and/or biological sensing [27,30] and whose "slow light" effect can be advantageous for increasing photocatalytic efficiencies [31,32].

The second point to underline is that O_2 affects the photophysical behavior of photogenerated charge carriers in photocatalytically active MOX materials. This is another field in which the PL analysis—especially when conducted in controlled environment conditions—can play a central role. In fact, PL monitors the recombination of charge carriers, while O_2 acts as an efficient electron scavenger, adsorbing on MOXs and producing charged species at the surface (mainly superoxide ions). These ions trigger the production of reactive oxide species and, importantly for the present discussion, modify (i.e., increase) the depth of the depletion region where the built-in electric field spatially separates the opposite charge carriers.

A schematic is proposed in Figure 1. Charge neutrality imposes the equality between the surface charge (negative in the example of Figure 1) and the bulk excess charge of opposite sign (represented as valence band holes in Figure 1). The latter is proportional to the depth D_{scr} of the space charge region, in which the radiative recombination of electrons and holes is hampered by the spatial separation of the opposite charges. PL experiments are hence sensitive to variation of D_{scr} in a range close to the optical penetration length, which can be as low as a few tenths of nanometers for PL experiments using above-bandgap excitation. In this sense, PL spectroscopy is not a surface-specific technique such as second harmonic generation [33,34], but is specifically sensitive to modifications of charge density occurring in the sub-surface region affected by the band bending [35–37].

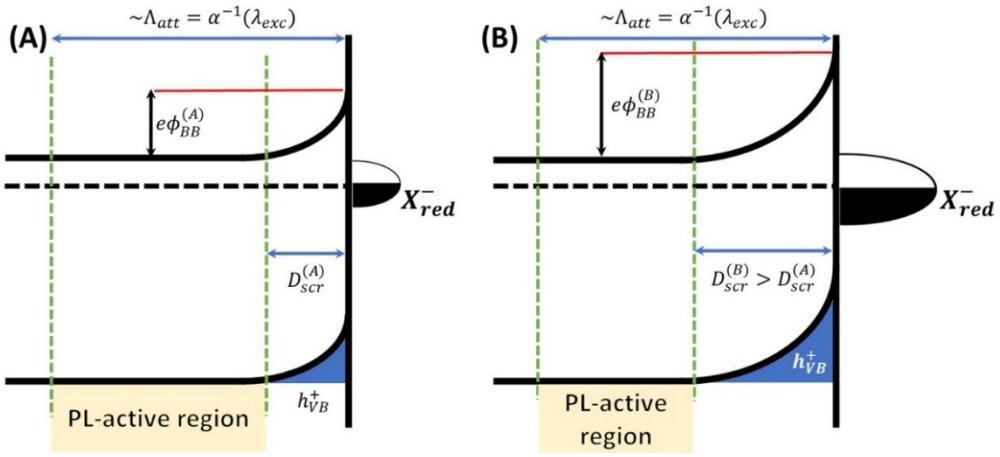

Figure 1. Schematic representation of the correlation between the PL-active sub-surface region and the surface concentration of chemisorbed ionic species, here indicated as X_{red} where "red" indicates a reduced species that traps free electrons. The surface concentration of chemisorbed species in panel (**A**) is lesser than in panel (**B**), which implies a thinner space charge region D_{scr}, lesser surface band bending energy $e\phi_{BB}$ and a wider PL-active region, in which opposite charge carriers are not spatially displaced. In both cases, free holes accumulate close to the surface to compensate the surface charge carried by chemisorbed electron-trapping species. The quantities Λ and α indicate the optical extinction length and the absorption coefficient at excitation wavelength, respectively.

The spatial extension of the depletion region decisively affects the migration of photogenerated charge carriers toward the catalyst surface. Hence, elucidating the effect of O_2 on the PL activity of photocatalytic MOXs also provides important information on how O_2 can affect the efficiency of photocatalytic reactions.

Previous studies highlighted the peculiar position of TiO_2 in the field of gas-sensitive luminescent MOXs. In particular, it is established that both PL enhancement and PL quenching can be induced by O_2, depending on the TiO_2 crystal phase [38,39]. This property appears to be a peculiar for TiO_2 and suggests that this material is the most interesting one among typical gas-sensitive MOXs for O_2 optochemical detection. However, the literature on chemosensors lacks comparative studies involving different MOX nanomaterials. Motivated by this consideration, we propose here a comparative study of TiO_2, ZnO and SnO_2 nanoparticles in relation to their ability to sense O_2 via PL modulation. These materials are chosen based on their importance in the field of chemosensors and on the fact that—to the best of the author's knowledge—the possibility of detecting O_2 by ZnO and SnO_2 has not been explored much.

While different physical methods can be employed to prepare gas-sensitive MOX nanoparticles [40–43], this work investigates nanoparticulated powders prepared by the same chemical route which is used to prepare thick film chemo-resistors, having the advantage of good production yields and well-established preparative procedures for the realization of stable devices [44–46].

2. Materials and Methods

2.1. Nanoparticles Preparations and Characterizations

Nanopowders of TiO_2, SnO_2 and ZnO were obtained through wet-chemical synthesis from reagent-grade starting materials used as received by the Merck Group supplier (Milan, Italy) mainly following the procedure described in References [47–49], respectively.

In summary, for TiO_2 preparation a solution of Ti(IV) n-butoxide in absolute ethanol was slowly added under stirring to an ethanol/water solution with a volume ratio of 1. After 10 min of stirring, the suspension was filtered by gravity, washed several times with water and diethyl ether, then dried at 100 °C overnight. The powders were calcined for 2 h at a temperature of 650 °C. This temperature was chosen on the basis of previous character-

izations [50] with the aim to obtain both anatase and rutile phases though maintaining a small crystallite size.

SnO_2 powders were prepared by adding drop-wise a small amount of deionized water to a 0.7 M n-butanol solution of Sn(II)2–ethylexanoate. By introducing HNO_3, the solution pH was found to be 1. Finally, the mixture was stirred for 3 h at room temperature. The resulting gel was filtered by gravity, washed several times with diethyl ether, dried at 100 °C overnight and calcined at 650 °C for 2 h.

ZnO synthesis started by preparing a 0.05 M water solution of $Zn(NO_3)_2$*$6H_2O$ to which was added ammonia hydroxide solution to reach a pH of 10. The solution was aged for 24 h at room temperature, then the white precipitate was filtered by gravity, washed with water and diethyl ether, and then it was dried in air at 100 °C overnight, and finally calcined for 2 h at 450 °C.

The morphology, the crystalline structure and the specific surface area (SSA) of the powders were studied by: (i) Field Scanning Electron Microscopy (FE-SEM) using a Carl Zeiss Sigma microscope operating at 3.00 kV, (ii) X-ray diffraction (XRD) analysis with a Philips PW 1830 vertical diffractometer in Bragg–Brentano geometry (PANalytical, formerly Philips Analytical, Almelo, The Netherland) (Cu Kα radiation, 40 kV, 30 mA) performing the Rietveld analysis with FullProf program (release 2011) and calculating the average crystallite size using the Scherrer's formula [a], and (iii) the Brunauer–Emmett–Teller (BET) method to the adsorption/desorption isotherms of N_2 at 77 K obtained with a Micromeritics ASAP 2010 physisorption analyzer.

2.2. Photoluminescence Measurements

PL measurements of MOX nanoparticulate at a tunable excitation wavelength in a controlled environment were performed by placing the samples in a home-built sealed stainless-steel test chamber equipped with a fused silica entrance optical window. Mixtures of dry N_2 (99.9995% purity) and dry air (20% O_2 and 80% N_2, 99.9995% purity) were flown in the test chamber during the measurements by mass flow control system. Optical excitation (~2 nm for the FWHM of the samples) was provided by a Xe lamp (450 W power) coupled with a double-grating excitation monochromator (Horiba Gemini, effective focal length = 180 mm) equipped with two 1200 grooves/mm gratings. The slit widths of the excitation monochromator were set up to obtain light centered at a desired wavelength with a spectral width (full width at half maximum) of about 3 nm. The monochromatized light was collected by a liquid waveguide and focused on the sample, which consisted of about 100 mg of nanoparticle powders lightly pressed into a steel washer to form a circular film of 0.7 cm diameter.

A system of converging lens and optical filters was employed to image the illuminated part of the sample on the input slit of a monochromator (Horiba Jobin-Yvon Triax 320, effective focal length 320 mm) collecting the PL emission and cutting off the excitation light. The PL spectra were obtained using a cooled CCD camera. The PL intensities are reported in counts per second (cps) units, which are the total counts of the digitally processed PL intensity as obtained by the CCD camera divided by the integration time. The entire system was controlled via a computer using a home-made LabView program.

3. Results

3.1. Structural and Morphological Characterizations

FE-SEM images (Figure 2) show a homogeneous distribution in particle size and a somewhat round shape for all materials. In particular, the grain dimension ranges from 20 to 40 nm for TiO_2 and SnO_2 and from 40 to 60 nm for ZnO. XRD patterns of the tree powders (Figure 3) confirm a pure single phase with the exceptions of TiO_2, for which there are both anatase (95%) and rutile (5%) phases, as expected. The crystalline phases (obtained from Rietveld refinement), the average crystallite sizes (evaluated by Scherrer's formula) and the calculated specific surface areas are summarized and reported in Table 1.

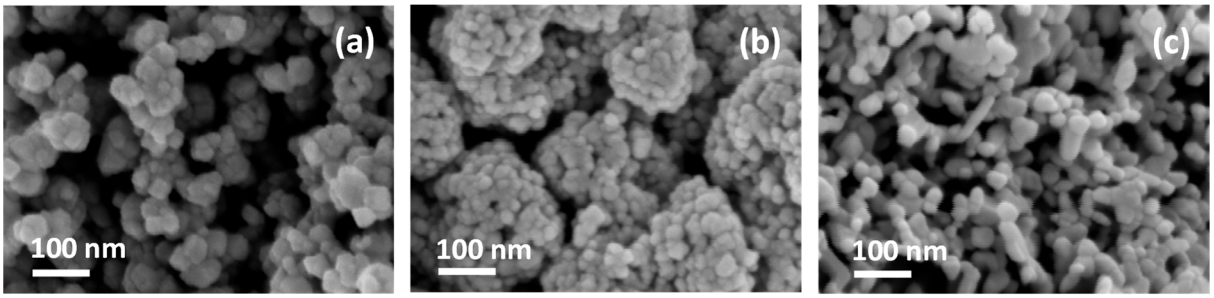

Figure 2. FE-SEM images of the TiO_2 (**a**) SnO_2 (**b**) and ZnO (**c**) powders.

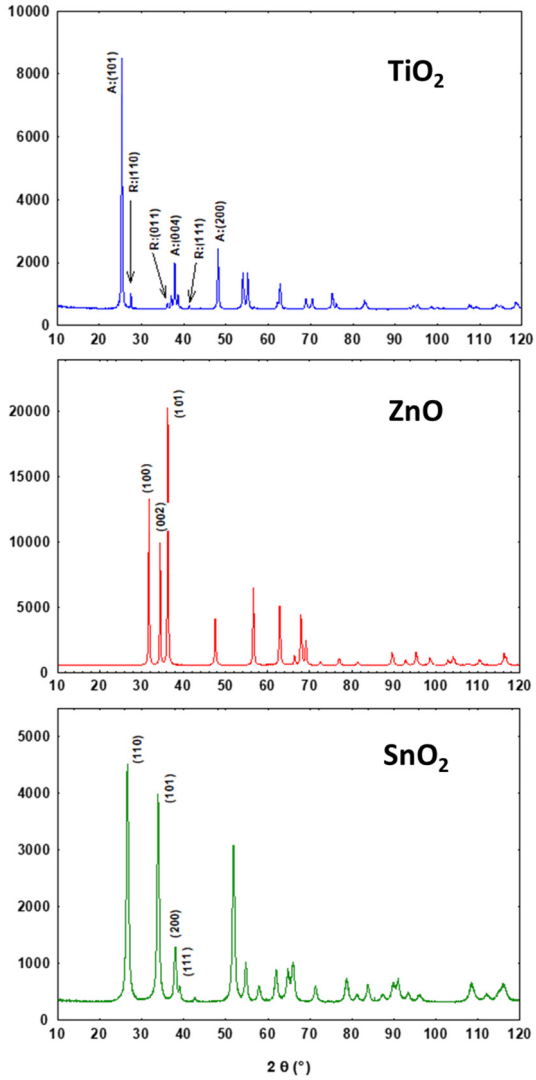

Figure 3. XRD intensities (reported in arbitrary units) for the investigated samples. Diffraction lines originating from anatase and rutile crystal planes of TiO_2 are evidenced in the top figure.

Table 1. Calcination temperatures, crystal size, specific surface area (SSA) and the composition of the TiO_2 powders (expressed in atomic percentages).

Sample	Calcination Temperature (°C)	Crystalline Phase	Composition (at. %)	Crystallite Sizes (nm)	SSA (m^2/g)
TiO_2	650	Rutile Anatase	5 95	61 34	29
ZnO	450	Wurtzite	100	33	12
SnO_2	650	Cassiterite	100	21	28

3.2. Photoluminescence Response towards O_2

The figures shown in this Section express the PL intensity of the samples measured vs. time as the sample is exposed to pure N_2 or to flowing N_2–air mixtures.

We start by presenting the results obtained for TiO_2 nanoparticles, which are by far the most interesting ones (as evidenced next).

A representative example of the results obtained using TiO_2 is shown in Figure 4, which reports the intensity map for the PL spectra acquired at excitation wavelength of 370 nm during exposures to pure N_2 (from t = 0 to t = 1200 s) and followed by exposures to air (and hence O_2) at different concentrations. Both visible and near-infrared PL emission (VIS-PL and NIR-PL, respectively) are observed. The two PL emission bands, centered at about 550 nm and 840 nm, originate from anatase and rutile phases of TiO_2, respectively [51].

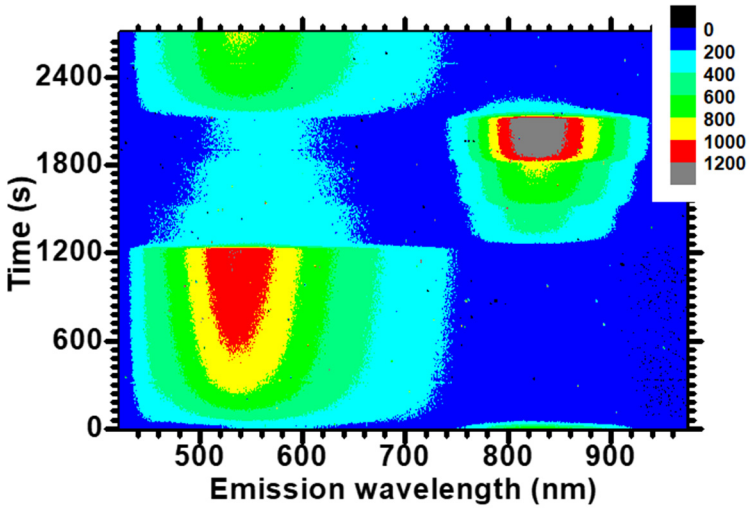

Figure 4. Intensity map of PL from TiO_2 (calcinated at 650 °C) acquired at different times during the experiment. Intensity is quantified in counts per seconds (cps) units. The air flow is activated at t = 1200 s (2% air concentration), 1500 s (4% air concentration) and 1800 s (10% air concentration), as also indicated in the next figure. During the first 1200 s and the last 600 s, the sample is kept under continuous illumination and N_2 flow. The data evidence clearly the anticorrelation between the VIS-PL intensity (which decreases during the interaction with O_2) and the NIR-PL intensity (which increases during the interaction with O_2). Excitation wavelength: 370 nm.

Air–N_2 mixtures at different (increasing) amounts of air concentration in Figure 4 have been inserted in the test chamber at times t = 1200 s (0.4% O_2 concentration), 1500 s (0.8% O_2 concentration) and 1800 s (2% O_2 concentration), preceded and followed by exposure to pure N_2 (i.e., in absence of O_2). The anti-correlated response to O_2 mentioned in the introduction is clearly evidenced.

The PL signal curves vs. gas exposure shown in the rest of the work have all been obtained from intensity data, as shown in Figure 4, by integrating the PL spectra over specified wavelength intervals $\Delta\lambda$, i.e.,

$$\text{PL signal}: \quad \Phi_{PL}(\lambda_{exc}, \Delta\lambda) = \int_{\Delta\lambda} I(\lambda_{exc}, \lambda_{PL}) d\lambda_{PL} \tag{2}$$

where $I(\lambda_{exc}, \lambda_{PL})$ is the PL intensity measured at wavelength λ_{PL} as the sample is excited at wavelength λ_{exc}. The different values used for the integration interval and the excitation wavelength are reported in the text and in the figure captions.

The data in Figure 5 show the wavelength-integrated PL intensity spectra for the TiO_2 sample (integrated over different wavelength intervals, namely $\Delta\lambda = 500$ nm $- 600$ nm for the VIS-PL (Figure 4A) and $\Delta\lambda = 800$ nm $- 900$ nm for the NIR-PL (Figure 4B).

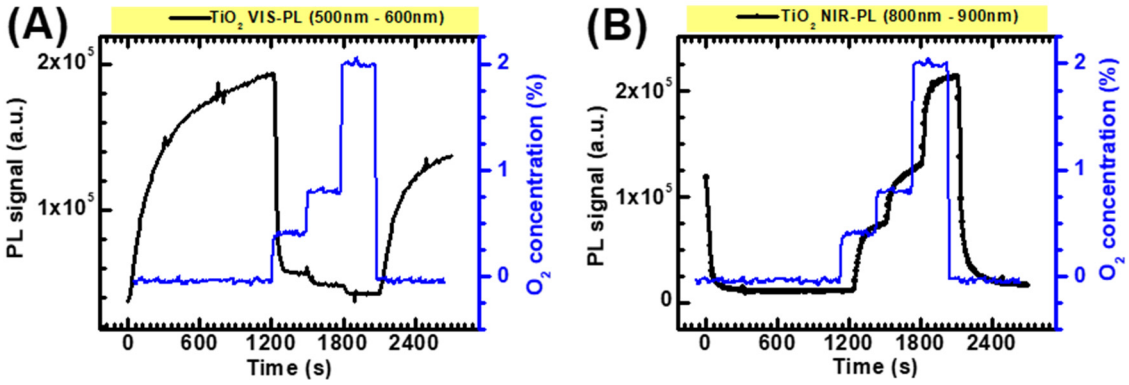

Figure 5. PL responses of TiO_2 to high O_2 concentrations. (**A**) Black curve: PL signal of TiO_2 integrated over the interval 500 nm–600 nm as a function of time. Blue curve: O_2 concentration in the air–N_2 flow. (**B**) Black curve: PL signal of TiO_2 integrated over the interval 800 nm–900 nm (NIR-PL) as a function of time. Blue curve: O_2 concentration in the air–N_2 flow. The investigated O_2 concentrations are 0.4%, 0.8% and 2%. During the first 20 min, the sample is kept under continuous illumination and exposure to nitrogen flow. Each air step has a duration of 5 min. The gas flow was kept constant at a flowing rate of 300 sccm. The O_2 concentrations are reported on the right axis in percent units.

During the first 20 min ("stabilization phase") the sample was kept under continuous illumination at a wavelength excitation of 370 nm and remained exposed to nitrogen flow. During this "stabilization" process in nitrogen, an O_2 desorption likely occurs as the sample was previously kept in natural air. Next, the gaseous flow was modified by introducing different amounts of dry air (namely 2%, 4% and 10%) leading to O_2 concentrations of 0.4%, 0.8% and 2%. The total flow was kept constant at a rate of 300 sccm during the entire measurement.

The stabilization phase in Figure 5A shows a VIS-PL enhancement during the O_2 desorption, i.e., indicates that O_2 quenches the VIS-PL at relatively high O_2 concentrations. It is to be noted that the PL variation is sub-linear vs. the O_2 concentration, i.e., the response saturates. This occurrence is not uncommon and can be explained in terms of saturation of a Langmuir-type saturation of available adsorption sites.

Considering then the NIR-PL results reported in Figure 5B, we see that the behavior is quite opposite to the one exhibited by the VIS-PL (as clearly visualized by the intensity map in Figure 4). In fact, the data obtained in the stabilization phase show a NIR-PL quenching during the O_2 desorption, thus indicating that O_2 enhances it. This is confirmed by the data obtained during the exposure to air. Interestingly, the NIR-PL responses are much more linear than the one observed previously for VIS-PL.

Additionally, it is important to note that (i): a complete stabilization is reached in a few minutes, which does not occur for the VIS-PL PL intensity, and (ii): as the 100% nitrogen flow is restored the PL signal almost completely reverts to the initial level. Both

these elements clearly evidence that the NIR-PL signal shows the better performance as an O_2-sensing parameter.

Given the interesting results obtained in Figure 5, the sample was tested also for exposure to low O_2 concentrations. The results are reported in Figure 6 for O_2 concentrations of 25, 50 and 75 ppm.

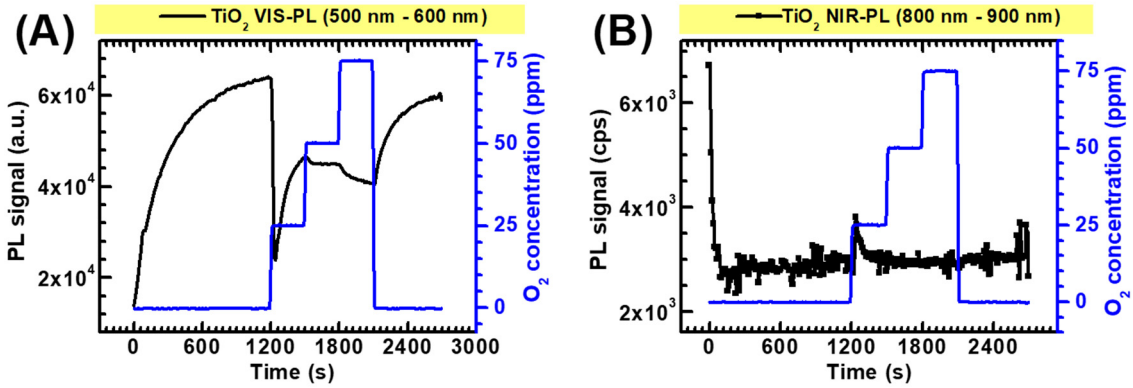

Figure 6. PL responses of TiO_2 to low O_2 concentrations. (**A**) Black curve: PL signal of TiO_2 integrated over the interval 500 nm–600 nm as a function of time. Blue curve: O_2 concentration in the air–N_2 flow. (**B**) Black curve: PL signal of TiO_2 integrated over the interval 800 nm–900 nm (NIR-PL) as a function of time. Blue curve: O_2 concentration in the air–N_2 flow. The investigated air concentrations are 25, 50 and 75 ppm. As in the previous case, the sample is kept under continuous illumination and exposure to nitrogen flow in the stabilization phase and each air step has a duration of 5 min. The gas flow was kept constant at a flowing rate of 300 sccm. The O_2 concentrations are reported on the right axis in part per million (ppm) units.

The data in Figure 6B indicate that the NIR-PL does not sense the O_2 concentrations in the range 25–75 ppm, except for a small response to the first O_2 step which is not replied at successive O_2 exposures. Additionally, for the VIS-PL (Figure 6A), the response to the first O_2 pulse is peculiar, as it produces a sudden decrease in the PL intensity which however recovers during the rest of the measurement, until the O_2 concentration is increased. When O_2 is changed to 50 ppm, a stable decrease is then observed, which is produced also for the successive change at 75 ppm of O_2 concentration.

Two elements can be underlined and discussed here: (i) the anomalous behavior immediately after the exposure to the first O_2 step (25 ppm) and (ii) the possibility to sense the O_2 at 50–75 ppm level using the VIS-PL. Instead, these concentrations have to be considered too low for detection via the rutile PL.

The comparative study was continued by testing nanoparticulated powders of SnO_2 and ZnO produced as previously described. These metal oxides are well established as the sensitive element of chemoresistive sensor devices and their PL response to NO_2 has also been studied in some works [52–55]. However, only very limited investigations of the potentialities of their PL response to O_2 have been published (to the best of our knowledge) [24,56]. The experimental results are summarized in Figure 7.

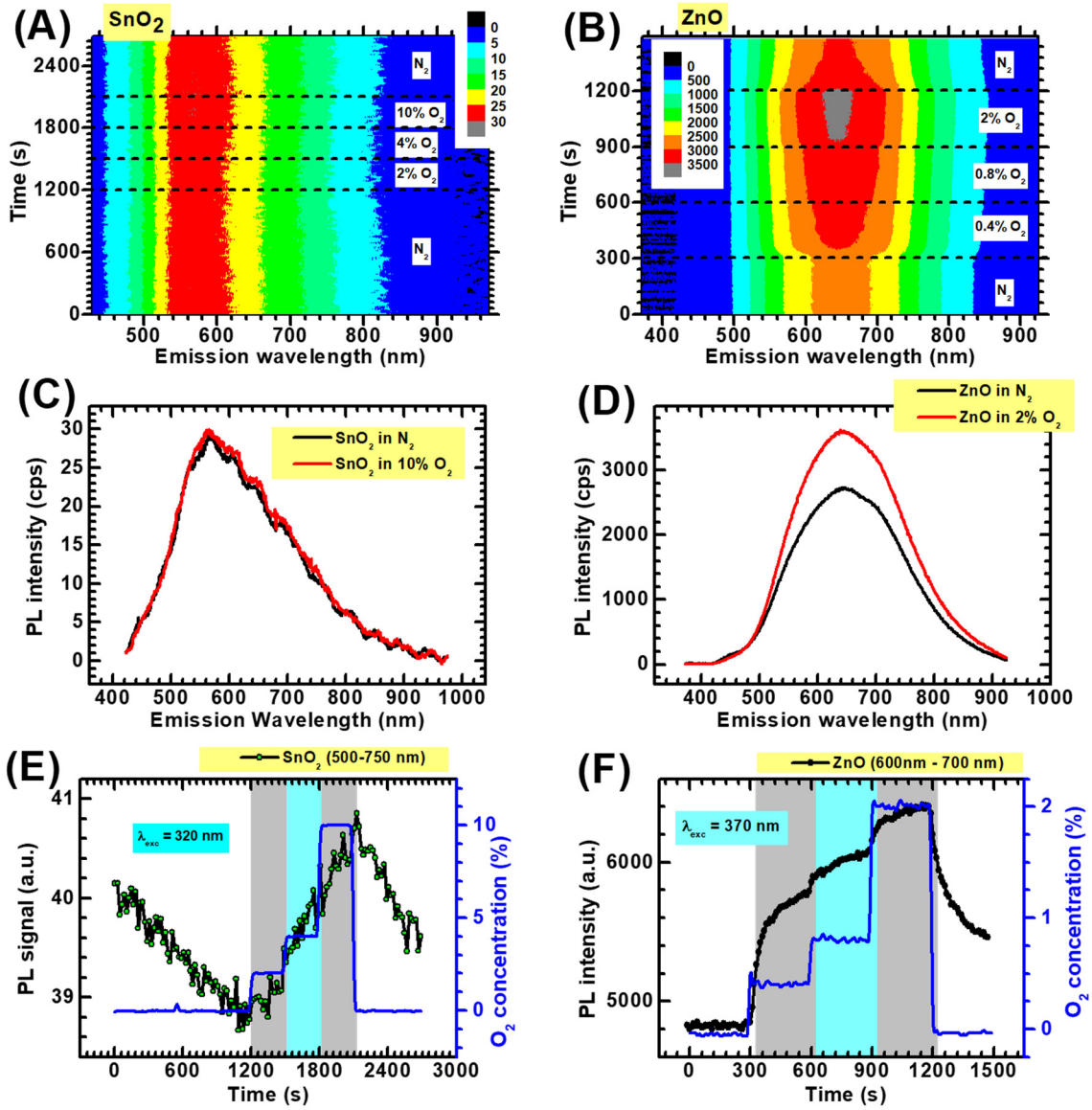

Figure 7. Results obtained for SnO_2 and ZnO nanoparticles. (**A**,**B**): PL intensity maps acquired for SnO_2 and ZnO (respectively) at different times during the experiment. Intensity is quantified in counts per seconds (cps) units. The dashed horizontal lines indicate the time at which the gaseous flow changes take place. The O_2 concentrations are also indicated in the figures. Excitation wavelengths were 320 nm for SnO_2 and 370 nm for ZnO. It is to be underlined that the air concentrations tested for the SnO_2 sample were different from those tested for ZnO and TiO_2, due to its lesser responsivity. (**C**,**D**): PL spectra for SnO_2 and ZnO acquired in N_2 once reached the stabilization (black curves) and at the maximum intensity in O_2 (red curves). (**E**,**F**): PL signal for SnO_2 (integrated over 500–750 nm interval) and ZnO (integrated over 600–700 nm interval). The O_2 concentrations are reported on the right axis in percent units.

The SnO_2 powder was characterized by a very weak PL intensity (approximately two orders of magnitudes lower than the one measured on ZnO sample in comparable conditions). The excitation spectra of SnO_2 and of ZnO are also significantly different, as the maximum PL intensity was obtained at a wavelength excitation of 320 nm for SnO_2 and 370 nm for ZnO. Such a difference correlates with the larger bandgap energy of SnO_2 (compared to the ZnO one).

Figure 7A,B show the PL intensity maps vs. time obtained for the SnO_2 and the ZnO sample, respectively. It can be immediately seen that the SnO_2 sample showed a much weaker PL emission, which was almost insensitive to O_2. Air exposures for Figure 7A,B occurred at different concentrations: higher air concentrations (10%, 20% and 50%) were

tested for SnO_2 due to the very weak response of the material. Other measurements at air concentrations of 2%, 4% and 10% were also performed on the sample (not shown here) and exhibited even less significant variations of the PL intensity.

The data in Figure 7B refer to ZnO. Compared to SnO_2, the latter shows a significant O_2-dependent PL intensity in the visible range. Here, the same air concentrations used in Figure 4 (i.e., 2%, 4% and 10%) were employed to favor a comparison with TiO_2.

Figure 7C,D show the stabilized PL spectra measured for SnO_2 and ZnO (respectively) in N_2 and in air (50% air for SnO_2, 10% air for ZnO). While any difference in the former is hardly recognizable, the latter exhibits a PL increase in 10% air that leaves the overall PL spectral shape unaltered, as also occurred for TiO_2. The result is interesting and somehow unexpected, as discussed in the next section.

The time dynamics of PL intensity for SnO_2 and ZnO upon air exposure are reported in Figure 7E,F for PL spectra integrated with wavelength intervals $\Delta\lambda = 500\ \text{nm} - 750\ \text{nm}$ and $\Delta\lambda = 600\ \text{nm} - 700\ \text{nm}$, respectively. The latter evidences the O_2-related PL enhancement with a saturating (sub-linear) response.

4. Discussion

The experimental results indicate that TiO_2 can be considered the most interesting material among the ones considered in this study for possible application as an O_2 optical sensor. The other oxides are less performing, but the experimental findings are nevertheless interesting from a scientific point of view. In fact, both SnO_2 and ZnO exhibit an O_2-induced enhancement, which in TiO_2 is observed only for the NIR-PL. This finding appears to be puzzling, as the mechanism schematized in Figure 1 would suggest for both SnO_2 and ZnO a PL quenching caused by the formation of surface charged species such as $O_2^{\bullet -}$ (superoxide ion), in accordance with the results obtained for anatase TiO_2. Therefore, the data lead us to discuss how the O_2 adsorption can cause either PL enhancement or PL quenching.

In this context, it is worth mentioning an interesting investigation by Ma and coworkers [57] who conducted PL measurements in controlled low-pressure O_2 conditions at low temperature, showing that the intensity of anatase PL can be either enhanced or quenched by exposure to molecular oxygen (O_2) depending on the O_2 dose. More precisely, they evidenced PL enhancement at low O_2 dosages and PL quenching at higher O_2 dosages and interpreted the data as a result of two O_2 adsorption mechanisms. At low O_2 pressures, a dissociative adsorption occurs at surface O vacancy sites, shrinking the depletion region (or, equivalently, decreasing the upward band bending). This increases the electron-hole spatial overlap and hence the PL efficiency. On the other hand, at higher O_2 partial pressures the relative amount of oxygen molecules with respect to available surface O vacancy sites also increases. Additional O_2 molecules are therefore adsorbed in the molecular form, forming superoxide species (e.g.,) enlarging the depletion region as shown in Figure 1 and hence quenching the PL intensity in a reversible way.

Even though the mechanism discussed by Ma and coworkers is sound, it appears to be incomplete. In fact, it describes the PL enhancement as caused by an irreversible bonding of O atoms with the (formerly reduced) lattice, while the only reversible mechanism (chemisorbed molecules) is associated with the PL quenching. In other words, it does not envisage the possibility of a reversible PL enhancement, which is indeed observed for rutile TiO_2. Furthermore, our data do not show O_2-induced enhancements of VIS-PL. Therefore, we conclude that additional explanations have to be proposed here.

The basic observation we propose here is that any PL emission which is enhanced by O_2 exposure shall arise from recombination of deeply trapped electrons characterized by a scarce mobility and not from free (conduction band) electrons. In fact, free electrons would be scavenged by O_2, leading to PL quenching according to the mechanism depicted in Figure 1. This basic observation is valid regardless of the chemical nature of the deeply trapped electron.

It has also to be observed that the O_2-induced PL enhancement strongly suggests that the energy of the involved trapped electrons is below the Fermi level (E_F), i.e., that trapped electrons are present at equilibrium, beforehand the UV illumination. The other possibility—i.e., energy levels of trapped electrons above E_F—conflicts with O_2-induced PL enhancement. In fact, an electron state with energy above E_F is empty at initial equilibrium and becomes occupied only during UV illumination via the relaxation of a photogenerated electron in conduction band. However, such a relaxation is clearly in competition against the scavenging of conduction band electrons by O_2, so that the net effect of oxygen adsorption would be to quench the PL intensity and not to enhance it.

As the O_2 adsorption favors both the migration of free (valence band) holes toward the surface (due to the upward band bending) and the PL emission, it is reasonable to propose that the trapped electrons causing the NIR-PL emission in rutile TiO_2 and the "red/orange" PL emission in ZnO are prevalently localized at the surface or sub-surface region. The resulting mechanism can be represented as in Figure 8.

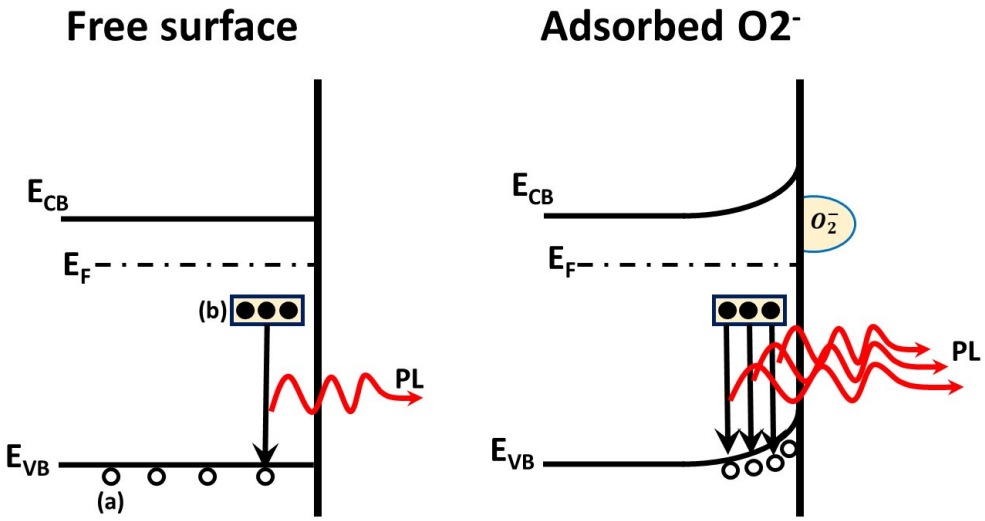

Figure 8. Possible scheme for O_2 enhanced PL emission. In the left figure the ideal case of a free surface with flat bands is represented. The white circles indicated as (**a**) are the photogenerated holes, while (**b**) indicates surface-localized deeply trapped electrons positioned below the Fermi level E_F. The energies E_{CB} and E_{VB} represent the edge of conduction and valence band, respectively. In the absence of adsorbed superoxide ions the photogenerated holes are (approximately) uniformly distributed within the PL-active region, so that the spatial overlap with the traps in (**b**) and the PL resulting from their recombination is not maximized. Once superoxide species are present, they induce the upward band bending reported on the right, fostering an accumulation of photogenerated holes close to the surface and enhancing the specific PL emission (such as the NIR-PL in TiO_2).

Clearly, the chemical identification of the electron-occupied defects of Figure 8 in the oxides that show O_2-enhanced PL is a subject that goes beyond the aim of this work. Here, only some suggestions can be discussed on that matter. Regarding the NIR-PL from rutile TiO_2, some works indeed argued that it shall be related to surface or sub-surface interstitial Ti^{3+} [58].

In regard to ZnO, Marotti and coworkers [59] performed a specific study on red-PL in ZnO, gathering evidence to suggest that it may be caused by the recombination of an electron in an intrinsic shallow state with a hole in an intrinsic deep state. They also proposed that the intrinsic deep state is also involved in the frequently observed green PL, which might be caused by the electronic transition from the conduction band to the mentioned deep state. Such a picture has been supported by an extensive study by Choi and coworkers [60], who indeed recognized (a): recombination between conduction electron and holes in singly ionized surface vacancy oxygen centers (indicated as $V_{O,S}^{+}$ in

their manuscript) and (b): recombination between shallow donors and $V_{O,S}^{+}$ as the origin of red PL [60]. This process in schematized in Figure 9.

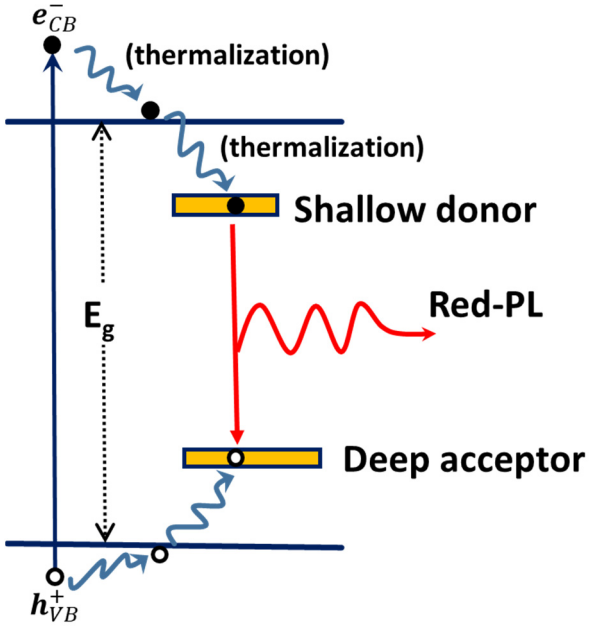

Figure 9. Model of red-PL of ZnO generated by above-bandgap excitation. Once the electron-hole pair is created, both the free charges thermalize to the available states with minimum (for electrons) and maximum (for holes) energy. Convincing studies (Ref. [60]) assigning the deep acceptor-like level (here indicated as "deep acceptor") to singly ionized surface oxygen vacancy centers are compatible with the observed enhancement caused by O_2 adsorption, in accordance with the arguments explained in the previous figure.

As discussed before, any surface accumulation of holes caused by O_2 adsorption is expected to favor the hole trapping at the deep defect, so that the recombination represented in the Figure 9 shall be favored in the presence of O_2. This possible mechanism suggests a surface nature of the deep defect: in this sense, it agrees with the work by Choi et al. However, its identification with $V_{O,S}^{+}$ cannot be stated with certainty only on the basis of our experimental findings.

5. Conclusions

To summarize, this work dealt with the effect exerted by molecular oxygen (O_2) adsorption on the photoluminescence (PL) of some metal oxides commonly used as sensitive elements of chemoresistive devices. We presented a comparative study of the PL response of SnO_2, ZnO and TiO_2 nanoparticles toward O_2. The metal-oxide nanoparticles were all prepared via sol–gel routes which are already established for the preparation of thick film chemosensors.

By subjecting the investigated samples to the same experimental procedures, very different results have been evidenced. SnO_2 exhibited virtually no response, while its PL efficiency was also found to be much lower than for the other oxides. ZnO nanoparticles exhibiting strong red/orange emission shown, surprisingly, an O_2-induced PL enhancement. TiO_2 exhibited by far the most interesting results, both in terms of sensitivity and versatility of the response. In particular, rutile TiO_2 is found to give a reversible and fast response for O_2 concentration in the range of relatively high O_2 concentrations (0.4–2%) in terms of its peculiar near-infrared PL emission. Anatase TiO_2 is instead found to be employable in lower concentrations ranges, manifesting sensitivity down to 25 ppm.

We argued that O_2-induced PL quenching is observed when the luminescence originates from free electrons, due to the enlargement of the depletion region and shrinking of

the PL-active volume. On another hand, PL enhancement likely originates from the recombination of surface-trapped electrons with free (e.g., Figure 8) or trapped (e.g., Figure 9) holes.

The experimental findings for NIR-PL of rutile TiO_2 suggest that its surfaces host deeply trapped electrons at large densities, so that a good sensitivity and, importantly, a relatively unsaturated response is obtained. The results thus indicate that a proper maximization of rutile TiO_2 surface area might well complement the anatase phase, so that a mixed phase nanoparticle system can be used to probe a wide range of O_2 concentrations.

We finally suggest that future work attempting to identify the chemical nature of deep defect states involved in the O_2-enhanced PL could proceed by computational quantum chemistry and by experiments on nanostructures with variable particle sizes and specific surface areas.

Author Contributions: Conceptualization: M.C.C. and S.L. Methodology: P.M. (Pietro Marani), M.C.C., P.M. (Pasqualino Maddalena) and S.L. Investigation: A.F., S.M., L.G. and S.L. Data curation: A.F., S.M., P.M. (Pietro Marani), L.G., P.M. (Pasqualino Maddalena), M.C.C. and S.L. Original draft preparation: S.L. Review and editing: M.C.C., P.M. (Pietro Marani) and P.M. (Pasqualino Maddalena). All authors have read and agreed to the published version of the manuscript.

Funding: This research was partially funded by Emilia-Romagna POR-FESR 2014-2020 project "EFFLICS-Eco Friendly Fluidics for Fluid Power"-CUP: F48D18000090009.

Institutional Review Board Statement: Not applicable.

Informed Consent Statement: Not applicable.

Data Availability Statement: Not applicable.

Conflicts of Interest: The authors declare no conflict of interest.

References

1. Preininger, C.; Klimant, I.; Wolfbeis, O.S. Optical Fiber Sensor for Biological Oxygen Demand. *Anal. Chem.* **1994**, *66*, 1841–1846. [CrossRef]
2. Crapo, J.D. Morphologic Changes in Pulmonary Oxygen Toxicity. *Annu. Rev. Physiol.* **1986**, *48*, 721–731. [CrossRef] [PubMed]
3. Mantell, L.L.; Lee, P.J. Signal Transduction Pathways in Hyperoxia-Induced Lung Cell Death. *Mol. Genet. Metab.* **2000**, *71*, 359–370. [CrossRef]
4. Pennacchietti, S.; Michieli, P.; Galluzzo, M.; Mazzone, M.; Giordano, S.; Comoglio, P.M. Hypoxia Promotes Invasive Growth by Transcriptional Activation of the Met Protooncogene. *Cancer Cell* **2003**, *3*, 347–361. [CrossRef]
5. Harris, A.L. Hypoxia–a Key Regulatory Factor in Tumour Growth. *Nat. Rev. Cancer* **2002**, *2*, 38–47. [CrossRef]
6. Ramamoorthy, R.; Dutta, P.K.; Akbar, S.A. Oxygen Sensors: Materials, Methods, Designs and Applications. *J. Mater. Sci.* **2003**, *38*, 4271–4282. [CrossRef]
7. Bittig, H.C.; Körtzinger, A.; Neill, C.; van Ooijen, E.; Plant, J.N.; Hahn, J.; Johnson, K.S.; Yang, B.; Emerson, S.R. Oxygen Optode Sensors: Principle, Characterization, Calibration, and Application in the Ocean. *Front. Mar. Sci.* **2018**, *4*. [CrossRef]
8. Quaranta, M.; Borisov, S.M.; Klimant, I. Indicators for Optical Oxygen Sensors. *Bioanal. Rev.* **2012**, *4*, 115–157. [CrossRef]
9. Amao, Y. Probes and Polymers for Optical Sensing of Oxygen. *Microchim. Acta* **2003**, *143*, 1–12. [CrossRef]
10. Wang, X.; Wolfbeis, O.S. Optical Methods for Sensing and Imaging Oxygen: Materials, Spectroscopies and Applications. *Chem. Soc. Rev.* **2014**, *43*, 3666–3761. [CrossRef]
11. Gehlen, M.H. The Centenary of the Stern-Volmer Equation of Fluorescence Quenching: From the Single Line Plot to the SV Quenching Map. *J. Photochem. Photobiol. C: Photochem. Rev.* **2020**, *42*, 100338. [CrossRef]
12. Xu, K.; Chen, Y.; Okhai, T.A.; Okhai, T.A.; Snyman, L.W. Micro Optical Sensors Based on Avalanching Silicon Light-Emitting Devices Monolithically Integrated on Chips. *Opt. Mater. Express OME* **2019**, *9*, 3985–3997. [CrossRef]
13. Lipka, T.; Moldenhauer, L.; Wahn, L.; Trieu, H.K. Optofluidic Biomolecule Sensors Based on A-Si:H Microrings Embedded in Silicon–Glass Microchannels. *Opt. Lett.* **2017**, *42*, 1084–1087. [CrossRef]
14. Coscia, U.; Ambrosone, G.; Lettieri, S.; Maddalena, P.; Rigato, V.; Restello, S.; Bobeico, E.; Tucci, M. Preparation of Microcrystalline Silicon–Carbon Films. *Sol. Energy Mater. Sol. Cells* **2005**, *87*, 433–444. [CrossRef]
15. Freeman, R.; Willner, I. Optical Molecular Sensing with Semiconductor Quantum Dots (QDs). *Chem. Soc. Rev.* **2012**, *41*, 4067–4085. [CrossRef] [PubMed]
16. Levitsky, I. Porous Silicon Structures as Optical Gas Sensors. *Sensors* **2015**, *15*, 19968–19991. [CrossRef]
17. Kim, H.-J.; Kim, Y.-Y.; Lee, K.-W. Multiparametric Sensor Based on DBR Porous Silicon for Detection of Ethanol Gas. *Curr. Appl. Phys.* **2010**, *10*, 181–183. [CrossRef]

18. Comini, E. Metal Oxide Nano-Crystals for Gas Sensing. *Anal. Chim. Acta* **2006**, *568*, 28–40. [CrossRef] [PubMed]
19. Ambrosone, G.; Coscia, U.; Lettieri, S.; Maddalena, P.; Minarini, C. Optical, Structural and Electrical Properties of Mc-Si:H Films Deposited by SiH4+H2. *Mater. Sci. Eng. B* **2003**, *101*, 236–241. [CrossRef]
20. Baratto, C.; Faglia, G.; Sberveglieri, G.; Gaburro, Z.; Pancheri, L.; Oton, C.; Pavesi, L. Multiparametric Porous Silicon Sensors. *Sensors* **2002**, *2*, 121–126. [CrossRef]
21. Setaro, A.; Bismuto, A.; Lettieri, S.; Maddalena, P.; Comini, E.; Bianchi, S.; Baratto, C.; Sberveglieri, G. Optical Sensing of NO2 in Tin Oxide Nanowires at Sub-Ppm Level. *Sens. Actuators B Chem.* **2008**, *130*, 391–395. [CrossRef]
22. Cretì, A.; Valerini, D.; Taurino, A.; Quaranta, F.; Lomascolo, M.; Rella, R. Photoluminescence Quenching Processes by NO_2 Adsorption in ZnO Nanostructured Films. *J. Appl. Phys.* **2012**, *111*, 073520. [CrossRef]
23. Mercado, C.; Seeley, Z.; Bandyopadhyay, A.; Bose, S.; McHale, J.L. Photoluminescence of Dense Nanocrystalline Titanium Dioxide Thin Films: Effect of Doping and Thickness and Relation to Gas Sensing. *ACS Appl. Mater. Interfaces* **2011**, *3*, 2281–2288. [CrossRef] [PubMed]
24. Sanchez-Valencia, J.R.; Alcaire, M.; Romero-Gómez, P.; Macias-Montero, M.; Aparicio, F.J.; Borras, A.; Gonzalez-Elipe, A.R.; Barranco, A. Oxygen Optical Sensing in Gas and Liquids with Nanostructured ZnO Thin Films Based on Exciton Emission Detection. *J. Phys. Chem. C* **2014**, *118*, 9852–9859. [CrossRef]
25. Pallotti, D.; Orabona, E.; Amoruso, S.; Maddalena, P.; Lettieri, S. Modulation of Mixed-Phase Titania Photoluminescence by Oxygen Adsorption. *Appl. Phys. Lett.* **2014**, *105*, 031903. [CrossRef]
26. Ricciardi, C.; Ballarini, V.; Galli, M.; Liscidini, M.; Andreani, L.C.; Losurdo, M.; Bruno, G.; Lettieri, S.; Gesuele, F.; Maddalena, P.; et al. Amorphous Silicon Nitride: A Suitable Alloy for Optical Multilayered Structures. *J. Non-Cryst. Solids* **2006**, *352*, 1294–1297. [CrossRef]
27. Passoni, L.; Criante, L.; Fumagalli, F.; Scotognella, F.; Lanzani, G.; Di Fonzo, F. Self-Assembled Hierarchical Nanostructures for High-Efficiency Porous Photonic Crystals. *ACS Nano* **2014**, *8*, 12167–12174. [CrossRef]
28. Yu, J.; Lei, J.; Wang, L.; Zhang, J.; Liu, Y. TiO2 Inverse Opal Photonic Crystals: Synthesis, Modification, and Applications—A Review. *J. Alloy. Compd.* **2018**, *769*, 740–757. [CrossRef]
29. Wu, Y.; Yang, W.; Fan, Y.; Song, Q.; Xiao, S. TiO_2 Metasurfaces: From Visible Planar Photonics to Photochemistry. *Sci. Adv.* **2019**, *5*, eaax0939. [CrossRef]
30. Terracciano, M.; Galstyan, V.; Rea, I.; Casalino, M.; De Stefano, L.; Sbervegleri, G. Chemical Modification of TiO_2 Nanotube Arrays for Label-Free Optical Biosensing Applications. *Appl. Surf. Sci.* **2017**, *419*, 235–240. [CrossRef]
31. Chiarello, G.L.; Zuliani, A.; Ceresoli, D.; Martinazzo, R.; Selli, E. Exploiting the Photonic Crystal Properties of TiO_2 Nanotube Arrays To Enhance Photocatalytic Hydrogen Production. *ACS Catal.* **2016**, *6*, 1345–1353. [CrossRef]
32. Likodimos, V. Photonic Crystal-Assisted Visible Light Activated TiO_2 Photocatalysis. *Appl. Catal. B: Environ.* **2018**, *230*, 269–303. [CrossRef]
33. Corn, R.M.; Higgins, D.A. Optical Second Harmonic Generation as a Probe of Surface Chemistry. *Chem. Rev.* **1994**, *94*, 107–125. [CrossRef]
34. Borbone, F.; Carella, A.; Caruso, U.; Roviello, G.; Tuzi, A.; Dardano, P.; Lettieri, S.; Maddalena, P.; Barsella, A. Large Second-Order NLO Activity in Poly(4-Vinylpyridine) Grafted with PdII and CuII Chromophoric Complexes with Tridentate Bent Ligands Containing Heterocycles. *Eur. J. Inorg. Chem.* **2008**, *2008*, 1846–1853. [CrossRef]
35. Stevanovic, A.; Ma, S.; Yates, J.T. Effect of Gold Nanoparticles on Photoexcited Charge Carriers in Powdered TiO_2 −Long Range Quenching of Photoluminescence. *J. Phys. Chem. C* **2014**, *118*, 21275–21280. [CrossRef]
36. Stevanovic, A.; Yates, J.T. Electron Hopping through TiO_2 Powder: A Study by Photoluminescence Spectroscopy. *J. Phys. Chem. C* **2013**, *117*, 24189–24195. [CrossRef]
37. Lettieri, S.; Pavone, M.; Fioravanti, A.; Santamaria Amato, L.; Maddalena, P. Charge Carrier Processes and Optical Properties in TiO_2 and TiO_2-Based Heterojunction Photocatalysts: A Review. *Materials* **2021**, *14*, 1645. [CrossRef] [PubMed]
38. Vequizo, J.J.M.; Kamimura, S.; Ohno, T.; Yamakata, A. Oxygen Induced Enhancement of NIR Emission in Brookite TiO_2 Powders: Comparison with Rutile and Anatase TiO_2 Powders. *Phys. Chem. Chem. Phys.* **2018**, *20*, 3241–3248. [CrossRef]
39. Lettieri, S.; Pallotti, D.K.; Gesuele, F.; Maddalena, P. Unconventional Ratiometric-Enhanced Optical Sensing of Oxygen by Mixed-Phase TiO_2. *Appl. Phys. Lett.* **2016**, *109*, 031905. [CrossRef]
40. Kaur, N.; Singh, M.; Moumen, A.; Duina, G.; Comini, E. 1D Titanium Dioxide: Achievements in Chemical Sensing. *Materials* **2020**, *13*, 2974. [CrossRef] [PubMed]
41. Preiß, E.M.; Rogge, T.; Krauß, A.; Seidel, H. Tin Oxide-Based Thin Films Prepared by Pulsed Laser Deposition for Gas Sensing. *Sens. Actuators B Chem.* **2016**, *236*, 865–873. [CrossRef]
42. Sanz, M.; López-Arias, M.; Marco, J.F.; de Nalda, R.; Amoruso, S.; Ausanio, G.; Lettieri, S.; Bruzzese, R.; Wang, X.; Castillejo, M. Ultrafast Laser Ablation and Deposition of Wide Band Gap Semiconductors. *J. Phys. Chem. C* **2011**, *115*, 3203–3211. [CrossRef]
43. Rella, R.; Spadavecchia, J.; Manera, M.G.; Capone, S.; Taurino, A.; Martino, M.; Caricato, A.P.; Tunno, T. Acetone and Ethanol Solid-State Gas Sensors Based on TiO_2 Nanoparticles Thin Film Deposited by Matrix Assisted Pulsed Laser Evaporation. *Sens. Actuators B Chem.* **2007**, *127*, 426–431. [CrossRef]
44. Morandi, S.; Fioravanti, A.; Cerrato, G.; Lettieri, S.; Sacerdoti, M.; Carotta, M.C. Facile Synthesis of ZnO Nano-Structures: Morphology Influence on Electronic Properties. *Sens. Actuators B Chem.* **2017**, *249*, 581–589. [CrossRef]

45. Fioravanti, A.; Bonanno, A.; Gherardi, S.; Carotta, M.C.; Skouloudis, A.N. A Portable Air-Quality Station Based on Thick Film Gas Sensors for Real Time Detection of Traces of Atmospheric Pollutants. *IOP Conf. Ser. Mater. Sci. Eng.* **2016**, *108*, 012005. [CrossRef]
46. Fioravanti, A.; Marani, P.; Massarotti, G.P.; Lettieri, S.; Morandi, S.; Carotta, M.C. (Ti, Sn) Solid Solution Based Gas Sensors for New Monitoring of Hydraulic Oil Degradation. *Materials* **2021**, *14*, 605. [CrossRef]
47. Carotta, M.C.; Fioravanti, A.; Gherardi, S.; Malagù, C.; Sacerdoti, M.; Ghiotti, G.; Morandi, S. (Ti,Sn) Solid Solutions as Functional Materials for Gas Sensing. *Sens. Actuators B Chem.* **2014**, *194*, 195–205. [CrossRef]
48. Morandi, S.; Amodio, A.; Fioravanti, A.; Giacomino, A.; Mazzocchi, M.; Sacerdoti, M.; Carotta, M.C.; Skouloudis, A.N. Operational Functionalities of Air-Quality W Sn Metal-Oxide Sensors Correlating Semiconductor Defect Levels and Surface Potential Barriers. *Sci. Total Environ.* **2020**, *706*, 135731. [CrossRef] [PubMed]
49. Fioravanti, A.; Marani, P.; Morandi, S.; Lettieri, S.; Mazzocchi, M.; Sacerdoti, M.; Carotta, M.C. Growth Mechanisms of ZnO Micro-Nanomorphologies and Their Role in Enhancing Gas Sensing Properties. *Sensors* **2021**, *21*, 1331. [CrossRef] [PubMed]
50. Carotta, M.C.; Gherardi, S.; Malagù, C.; Nagliati, M.; Vendemiati, B.; Martinelli, G.; Sacerdoti, M.; Lesci, I.G. Comparison between Titania Thick Films Obtained through Sol–Gel and Hydrothermal Synthetic Processes. *Thin Solid Film.* **2007**, *515*, 8339–8344. [CrossRef]
51. Pallotti, D.K.; Orabona, E.; Amoruso, S.; Aruta, C.; Bruzzese, R.; Chiarella, F.; Tuzi, S.; Maddalena, P.; Lettieri, S. Multi-Band Photoluminescence in TiO_2 Nanoparticles-Assembled Films Produced by Femtosecond Pulsed Laser Deposition. *J. Appl. Phys.* **2013**, *114*, 043503. [CrossRef]
52. Baratto, C.; Comini, E.; Faglia, G.; Sberveglieri, G.; Zha, M.; Zappettini, A. Metal Oxide Nanocrystals for Gas Sensing. *Sens. Actuators B Chem.* **2005**, *109*, 2–6. [CrossRef]
53. Trani, F.; Causà, M.; Lettieri, S.; Setaro, A.; Ninno, D.; Barone, V.; Maddalena, P. Role of Surface Oxygen Vacancies in Photoluminescence of Tin Dioxide Nanobelts. *Microelectron. J.* **2009**, *40*, 236–238. [CrossRef]
54. Valerini, D.; Cretì, A.; Caricato, A.P.; Lomascolo, M.; Rella, R.; Martino, M. Optical Gas Sensing through Nanostructured ZnO Films with Different Morphologies. *Sens. Actuators B Chem.* **2010**, *145*, 167–173. [CrossRef]
55. Orabona, E.; Pallotti, D.; Fioravanti, A.; Gherardi, S.; Sacerdoti, M.; Carotta, M.C.; Maddalena, P.; Lettieri, S. On Mechanism of NO_2 Detection by ZnO Excitonic Luminescence. *Sens. Actuators B Chem.* **2015**, *210*, 706–711. [CrossRef]
56. Lin, Y.; Wang, D.; Zhao, Q.; Li, Z.; Ma, Y.; Yang, M. Influence of Adsorbed Oxygen on the Surface Photovoltage and Photoluminescence of ZnO Nanorods. *Nanotechnology* **2006**, *17*, 2110–2115. [CrossRef]
57. Ma, S.; Reish, M.E.; Zhang, Z.; Harrison, I.; Yates, J.T. Anatase-Selective Photoluminescence Spectroscopy of P25 TiO_2 Nanoparticles: Different Effects of Oxygen Adsorption on the Band Bending of Anatase. *J. Phys. Chem. C* **2017**, *121*, 1263–1271. [CrossRef]
58. Santara, B.; Giri, P.K.; Imakita, K.; Fujii, M. Evidence for Ti Interstitial Induced Extended Visible Absorption and Near Infrared Photoluminescence from Undoped TiO_2 Nanoribbons: An In Situ Photoluminescence Study. *J. Phys. Chem. C* **2013**, *117*, 23402–23411. [CrossRef]
59. Marotti, R.E.; Badán, J.A.; Quagliata, E.; Dalchiele, E.A. Red Photoluminescence and Band Edge Shift from ZnO Thin Films. *Phys. B: Condens. Matter* **2007**, *398*, 337–340. [CrossRef]
60. Choi, S.; Phillips, M.R.; Aharonovich, I.; Pornsuwan, S.; Cowie, B.C.C.; Ton-That, C. Photophysics of Point Defects in ZnO Nanoparticles. *Adv. Opt. Mater.* **2015**, *3*, 821–827. [CrossRef]